ACS APPLIED MATERIALS & INTERFACES

Research Article

www.acsami.org

Hierarchical SnO_2 Nanostructures Made of Intermingled Ultrathin Nanosheets for Environmental Remediation, Smart Gas Sensor, and Supercapacitor Applications

Yang Liu,[†] Yang Jiao,[†] Zhenglin Zhang,[†] Fengyu Qu,[†] Ahmad Umar,*[,‡,§] and Xiang Wu*[,†]

[†]Key Laboratory for Photonic and Electronic Bandgap Materials, Ministry of Education and College of Chemistry and Chemical Engineering, Harbin Normal University, Harbin 150025, P. R. China

[‡]Promising Centre for Sensors and Electronic Devices (PCSED) and [§]Department of Chemistry, College of Science and Arts, Najran University, Najran 11001, Kingdom of Saudi Arabia

Supporting Information

ABSTRACT: In this paper, the hierarchical SnO_2 nanostructures (HTNs) were prepared by a facile hydrothermal process. The prepared HTNs were characterized in detail by various analytical techniques that reveal the well-crystallinity with tetragonal rutile structure of SnO_2 for the as-prepared material. By detailed experiments, interestingly, it was observed that the shapes and sizes of as-prepared HTNs could be tailored by varying the precursor concentration and reaction time. The synthesized HTNs were used as the efficient photocatalysts for the photocatalytic degradation of methylene blue (MB) under light illumination which showed almost complete degradation (~99%) of MB dye in 20 min. The observed degradation for MB dye was higher than other commonly used dyes, i.e. methyl orange (MO; 96% in 50 min) and Rhodamine B (RhB; 97% in 40 min.). Further, the prepared HTNs were used as the effective gas sensing material to examine a series of volatile gases, such as ethanol, ammonia, benzene, acetone, toluene, methanol, diethyl ether, and methanol. By the detailed experiments, it was observed that the prepared HTNs exhibited tremendous gas sensing performance toward ethanol. Finally, because of the unique morphology and the fast ion and electron transfer characteristics, the prepared HTNs show excellent supercapacitor performances.

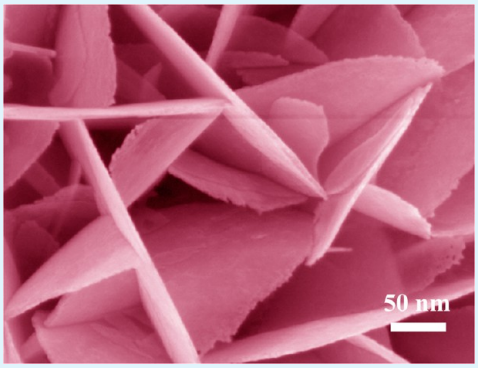

KEYWORDS: *SnO_2 nanostructures, ultrathin nanosheets, environmental remediation, gas sensor, supercapacitor*

1. INTRODUCTION

Metal oxide nanomaterials are presenting themselves as one of the most important class of materials due to their excellent properties and wide applications in various areas of science and technology.[1] Among various metal oxide nanomaterials, tin dioxide (SnO_2) is one of the smart materials because of its own exotic properties and broad range of applications.[2−6] Due to the excellent properties of SnO_2 such as wide band gap (E_g = 3.6 eV, at 300 K), electrical, optical and high chemical stability and so on, the SnO_2 is widely used for various high-technological applications to name a few, chemical and gas sensors, biosensors, dye-sensitized solar cells, optical waveguides, field effect transistors, lithium-ion batteries and supercapacitors, photocatalysts, transparent electrodes, and so on.[7−17] It is proven that the chemical and physical properties of SnO_2 nanomaterials are greatly affected by the geometrical factors and surface area.[18] Therefore, it is highly important to construct special morphological moieties which possess higher surface to volume ratio and hence show better reactivity. In this direction, the construction of 2D and 3D SnO_2 morphologies have attracted much more attention as these classes of materials can possess higher surface area and exhibit better reactivity toward various applications such as photocatalysis, sensing, supercapacitors, etc. Recently, Gao et al. have demonstrated the synthesis and efficient gas sensing properties of 3D SnO_2 microstructures assembled by porous nanosheets.[19] Wang et al. have prepared SnO_2 powders with various morphologies and used the synthesized materials for photocatalytic applications.[20] Latterly, Meng and co-workers have demonstrated the growth of SnO_2 nanoflowers for supercapacitor applications.[21] Previously, Chen et al. have prepared 3D SnO_2 nanoflowers with nanoporous petals using a controlled structure-preserving thermal oxidation process.[22] Zhang et al. have also reported the growth and field emission applications of sunflowerlike SnO_2 nanoflowers on silicon substrates using vapor phase transport method.[23] Poppy flowerlike SnO_2 nanoflower array on Sn-foil by solvothermal method was reported by Ghosh et al.[24] There are many other reports in the literature that demonstrate the growth, properties, and applications of flowerlike nanostructures assembled from nanosheets.[25,26] You et al. reported a

Received: November 22, 2013
Accepted: January 20, 2014
Published: January 20, 2014

novel and symmetric SnO_2 structures prepared in a solution reaction system with DMF as a solvent and investigated their photocatalytic activity.[27] Chen and co-workers synthesized SnO_2 nanopolyhedrons assembled from ultrathin SnO_2 nanowires by sodium dodecyl sulfate (SDS) assisted hydrothermal process and studied their gas-sensing properties.[28] Pusawale's group prepared nanocrystalline SnO_2 thin films on glass and stainless steel substrates and investigated their supercapacitor performance.[29] Even though several reports have been published for the growth of 3D SnO_2 nanomaterials in the literature, most of them follow very complicated and tedious experimental procedure and cause pollution.[30,31]

In this paper, a simple hydrothermal approach is proposed to prepare novel 3D hierarchical SnO_2 nanostructures (HTNs). The prepared HTNs were investigated in detail in terms of their morphological, structural, compositional, and optical properties. Moreover, systematic experiments were performed to understand the step-by-step formation of the prepared hierarchical nanostructures. For application point of view, the prepared HTNs were used as the efficient photocatalyst for the photocatalytic degradation of methylene blue (MB), methyl orange (MO), and rhodamine B (RhB) under UV light irradiation. Moreover, the prepared HTNs were used for the fabrication of efficient, highly sensitive and selective ethanol gas sensors. Finally, the prepared HTNs were used for the fabrication of supercapacitor and the results demonstrating the outstanding rate capability and high reversibility with little capacitance loss for the prepared nanomaterials.

2. EXPERIMENTAL SECTION

2.1. Synthesis of Hierarchical SnO_2 Nanostructures Made of Intermingled Ultrathin Nanosheets. The HTNs were prepared by facile hydrothermal process using easy available laboratory chemicals. For the synthesis of HTNs, all the chemicals were analytical grade and used as received without further purification. In a typical reaction process, 5 mmol $SnCl_2{\cdot}2H_2O$, and 10 mmol $C_6H_5Na_3O_7{\cdot}2H_2O$ were added into 40 mL of an ethanol−water (1:1) solution under vigorous stirring for 1 h. After stirring, the resultant solution was loaded into a Teflon-lined stainless steel autoclave, sealed, and heated to 180 °C for 8 h. After completing the reaction, the autoclave was naturally cooled to room temperature and the obtained product was finally washed with DI water and ethanol sequentially. Further, the obtained product was annealed at 600 °C for 2 h. To examine the effect of precursor concentrations, various experiments were performed by varying the molar ratios of $SnCl_2{\cdot}2H_2O$ and $C_6H_5Na_3O_7.2H_2O$, and it was observed that by varying the precursors concentrations, the morphologies and sizes of the prepared nanomaterials can be controlled.

2.2. Characterizations of Hierarchical SnO_2 Nanostructures Made of Intermingled Ultrathin Nanosheets. The prepared HTNs were examined in terms of their structural, morphological, compositional, optical, and specific surface area properties. To examine the crystal quality and crystallinity, the prepared HTNs were examined by X-ray diffractometer (XRD, Rigaku Dmax-2600/pc, Cu K radiation, λ = 0.1542 nm, 40 KV, 150 mA). The detailed morphologies of the samples were characterized by field-emission scanning electron microscope (FESEM, Hitachi-4800) and transmission electron microscope (TEM, JEOL-2010) equipped with high-resolution TEM (HRTEM). The microstructural characteristics were analyzed by Raman spectroscopy (LabRAM HR 800). The chemical and elemental compositions of the prepared HTNs were checked by Fourier transform infrared (FTIR; Perkin-Elmer) spectroscopy and energy-dispersive spectroscopy (EDS), attached with FESEM, respectively. The optical properties were investigated by photoluminescence spectroscopy (HORIBA JY-Fluoro Max 4) at room temperature. The specific surface area of the prepared material was estimated using the Brunauer−Emmett−Teller (BET) equation based on the nitrogen adsorption isotherm obtained with a Belsorp-max. The pore size distribution was determined with the Barrett−Joyner−Halenda (BJH) method applied to the desorption branch of adsorption−desorption isotherm.

2.3. Photocatalytic Decomposition of Organic Dyes Using Hierarchical SnO_2 Nanostructures Made of Intermingled Ultrathin Nanosheets. The photocatalytic degradation of organic dyes (MB, MO, and RhB) was done by using the prepared HNTs as the photocatalysts under light illumination. For the photocatalytic experiments, 0.1 g of HTNs were suspended in 200 mL of 40 mg L^{-1} of organic dye aqueous solutions. The solutions were persistently stirred for 1 h in the dark to establishment the adsorption−desorption equilibrium among HTNs, organic dyes and water. Consequently, the resultant solutions were exposed to UV irradiation from a mercury lamp (500 W) at room temperature. The photocatalytic degradation of the organic dyes was estimated by measuring the absorbance of dye solution in the presence of photocatalyst exposed at different time intervals (5 min). The degradation efficiencies of the organic dyes were analyzed by monitoring the dye decolorization at the maximum absorption wavelength using UV−vis spectrophotometer (Shimazu UV-2550).

2.4. Fabrication and Characterization of Gas Sensors Using Hierarchical SnO_2 Nanostructures Made of Intermingled Ultrathin Nanosheets. For the gas sensing measurements, the prepared HTNs were mixed with deionized water to form a paste. The sensors were made by coating ceramic tube with the paste to form a thin sensing film. A pair of gold electrodes was installed at each end of the ceramic tube before it was coated with the paste. Further, each electrode was connected with two Pt wires. A Ni−Cr heating wire was inserted into the tube to form an indirect-heated gas sensor. The surface of sensor was stabilized by heating the sensor element at 450 °C for 3 h in air to improve the mechanical strength.

2.5. Electrochemical Properties of Hierarchical SnO_2 Nanostructures Made of Intermingled Ultrathin Nanosheets. Electrochemical characteristics of the as-obtained products were studied on an CHI660 electrochemical workstation (Chenhua, Shanghai) using cyclic voltammetry, chronopotentiometry and electrochemical impedance test by configuring the samples into a three electrodes cell, where the samples were used as the working electrode, Pt foil as the counter electrode and a saturated calomel electrode (SCE) as the reference electrode. The working electrodes were prepared as follows: the electrode of the obtained SnO_2 microspheres was prepared according to the following steps. A mixture containing 80 wt % SnO_2 microspheres, 15 wt % acetylene black, and 5 wt % polytetrafluoroethylene (PTFE) was well mixed and dried under a vacuum at 120 °C for 5 h, the electrode area is 1 cm^2, and the loading density is about 8.0 mg cm^{-2}. The electrolyte used was 1 M Na_2SO_4 aqueous solution as an electrolyte at room temperature. The electrochemical properties and capacitive behavior of the supercapacitor electrodes were evaluated by cyclic voltammetry (CV) and galvanostatic charge−discharge (CD).

The specific capacitance, C (F g^{-1}), of the electrode material was calculated from the galvanostatic discharge according to the following equation

$$C = I\Delta t/(\Delta V m)$$

where I is the discharge current (A), Δt is the discharge time (s), ΔV is the voltage change (V) excluding IR drop in the discharge process, and m is the mass of the active material (g). The electrochemical impedance spectroscopy (EIS) measurements were performed by applying an AC voltage with 5 mV amplitude in a frequency range from 0.01 Hz to 100 kHz.

3. RESULTS AND DISCUSSION

3.1. Detailed Structure Characterizations of Hierarchical SnO_2 Nanostructures Made of Intermingled Ultrathin Nanosheets. To examine the crystallinity and crystal phases, the prepared HTNs were analyzed by X-ray diffraction pattern. Figure 1a shows the typical XRD patterns of the

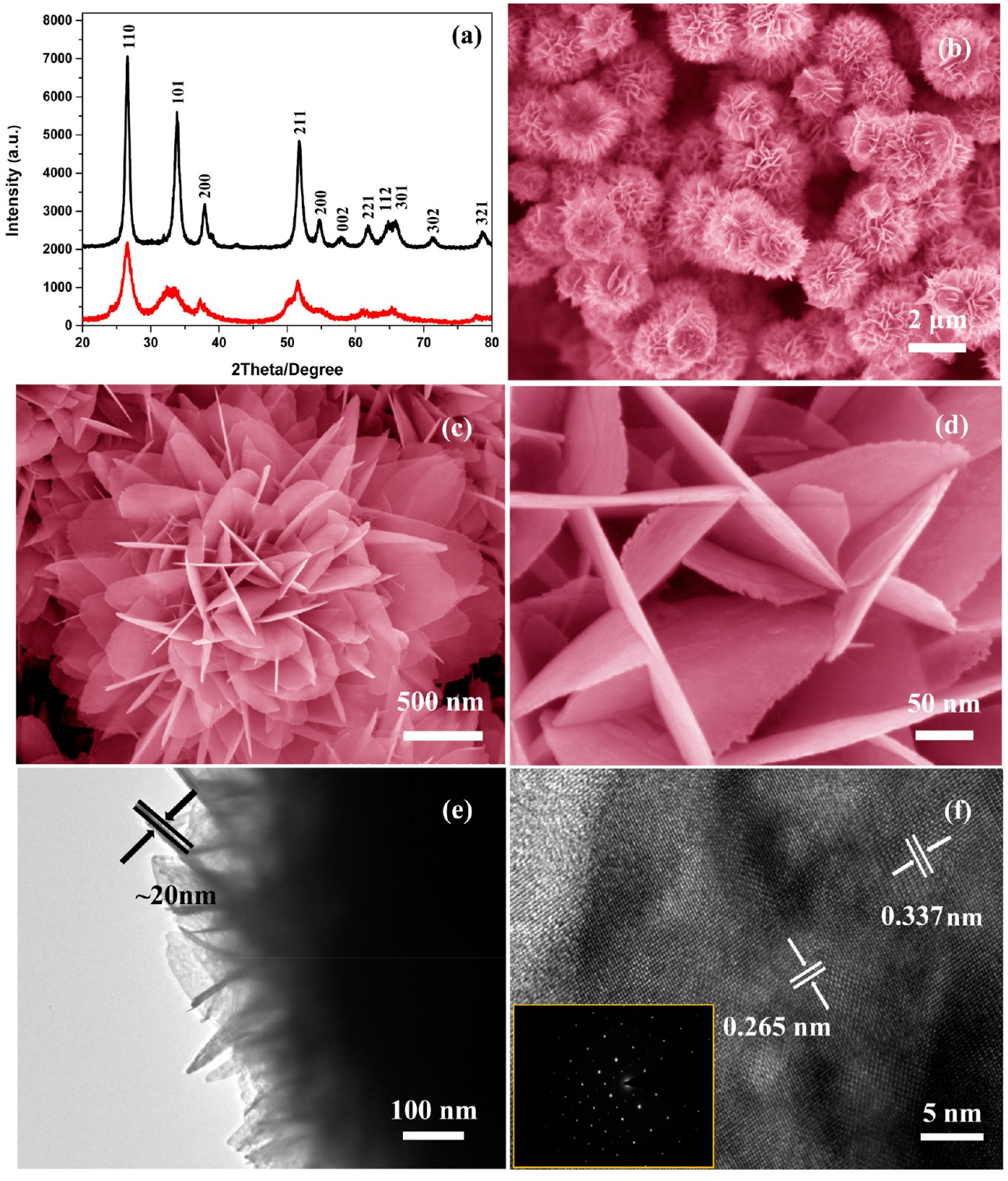

Figure 1. (a) Typical XRD patterns of the prepared SnO_2 architectures before (red line) and after calcination (black line); (b–d) FESEM images, (e) low-magnification TEM image, and (f) high-resolution TEM (HRTEM) image of the prepared hierarchical SnO_2 nanostructures. Inset in f exhibits the typical corresponding SAED pattern.

prepared SnO_2 architectures before (red line) and after calcination (black line). Interestingly, it was observed that the XRD pattern of the calcined sample (black line) exhibited sharper and clearer diffraction peaks as compared to uncalcined sample which indicate that the crystallinity of the sample increased after calcination. All the observed diffraction peaks are indexed to tetragonal rutile structure of pure SnO_2 and matched with JCPDS Card (no. 41–1445). Except for SnO_2, no other diffraction reflections were detected in the pattern, which further confirms that the prepared samples are well-crystalline and pure SnO_2.

The general morphologies of the prepared SnO_2 materials were investigated by FESEM and the results are demonstrated in Figure 1b–d. As confirmed by the FESEM observations that

dx.doi.org/10.1021/am405301v | ACS Appl. Mater. Interfaces 2014, 6, 2174–2184

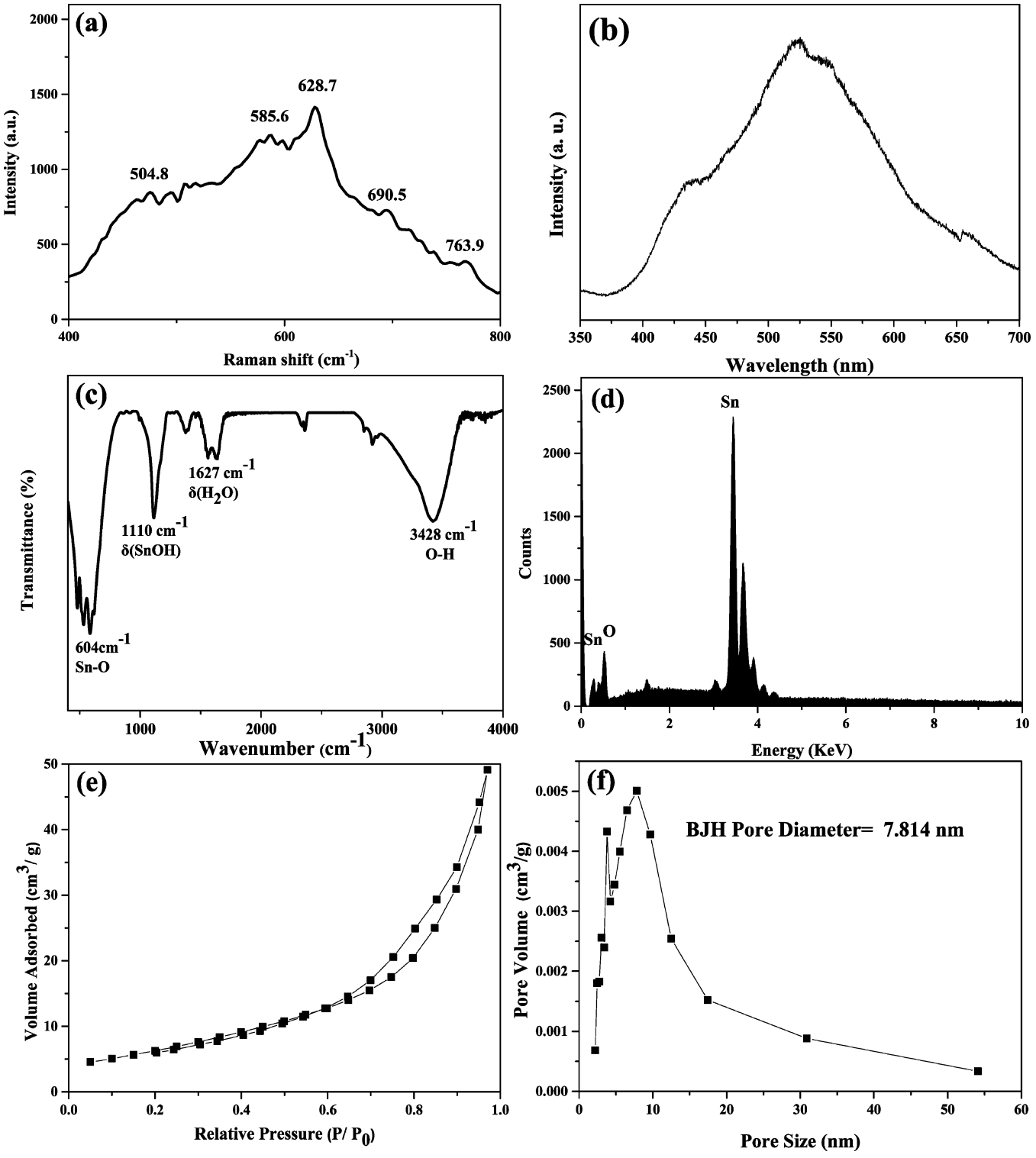

Figure 2. (a) Typical Raman-scattering spectrum; (b) room-temperature photoluminescence spectrum; (c) T FT-IR spectrum; (d) EDS spectrum; (e) typical nitrogen adsorption−desorption isotherm; and (f) BJH pore size distribution plots of the prepared hierarchical SnO_2 nanostructures.

the prepared material possess hierarchical flower-shaped morphologies and grown in very high density (Figure 1b). The typical diameter of a single hierarchical flower-shaped morphology was ~3 ± 1 μm. Interestingly, it was observed that the hierarchical flower-shaped structures are made of ultrathin nanosheets which intermingle with each other in such a manner that one corner of individual nanosheet is connected with the side surface of the nanosheet and hence made almost triangular shaped morphologies (Figure 1c, d). Fascinatingly, the nanosheets possess smooth and clean surfaces throughout their diagonal with the typical thickness of ~17 ± 3 nm. The detailed morphological and structural characterizations of the prepared material were examined by TEM equipped with HRTEM and selected area electron diffraction (SAED) pattern.

Figure 1e exhibits the typical TEM image of the prepared hierarchical structures which reveals the full consistency with

dx.doi.org/10.1021/am405301v | ACS Appl. Mater. Interfaces 2014, 6, 2174−2184

the observed FESEM results in terms of shape and sizes. The typical thickness of the nanosheets was ~20 nm. The detailed structural and crystallographic properties of the HTNs were examined by high-resolution TEM (HRTEM) and SAED pattern which confirmed the high-crystalline nature of the prepared material. The HRTEM image exhibits the well-defined lattice fringes with the lattice spacing of 0.337 and 0.265 nm, which correspond to the (110) and (101) lattice planes of SnO_2, respectively (Figure 1f). Inset in Figure 1f exhibits the typical SAED pattern of the corresponding material, which confirmed that the prepared nanosheets are well-crystalline.

Raman scattering spectroscopy is one of the powerful techniques that provide the detailed microstructural properties of semiconductor materials. Therefore, the prepared HTNs were examined by Raman-scattering spectroscopy. The rutile SnO_2 crystal belongs to D_{4h}^{14} point group and $P4_2/mnm$ space group. Based on the group theory, the normal lattice vibration modes of single-crystal SnO_2 at the Γ point of the Brillouin zone can be written as follows.[30]

$$\Gamma = A_{1g}(R) + A_{2g}(F) + A_{2u}(IR) + B_{1g}(R) + B_{2g}(R) + 2B_{1u}(F) + E_g(R) + 3E_u(IR)$$

Where E_g, A_{1g}, and B_{1g} modes are Raman active, whereas B_{2g} and E_g represent vibration modes with displacement in the direction of the *c*-axis, A_{1g} and B_{1g} demonstrate the vibrations with displacements perpendicular to the *c*-axis and B_{2g} presents asymmetric Sn−O stretching of SnO_2. Seven modes of A_{2u} and $3E_u$ are IR active and two modes of A_{2g} and B_{1u} are inactive.

Figure 2a exhibits the typical Raman spectrum of the prepared HTNs measured at room temperature. As shown in Figure 2a, the peaks at 474.8, 628.7, 690.5, and 763.9 cm^{-1} are attributed to the E_g, A_{1g}, $(A_{2u})V_{(LO)}$, and B_{2g} vibration modes, respectively, which are related to the symmetric and asymmetric stretching vibration modes of Sn−O bonds. These peaks are in good agreement with the bulk SnO_2 materials reported in the literature.[31] Besides, an additional Raman scattering peak are also seen in the spectrum at 585.6 cm^{-1}, which may be attributed to small granule size, leading to vacant lattice sites and local lattice disorder such as individual oxygen vacancies and their complexes in the product.[32,33] Therefore, the presence of significant Raman-scattering peaks in the spectrum confirmed that the prepared HTNs are well-crystalline and possess tetragonal rutile structure.

The optical properties of the prepared HTNs were examined by room temperature photoluminescence (PL) spectroscopy. Figure 2b shows the typical room temperature PL spectrum of the prepared HTNs. The band-to-band emission peak of the SnO_2 nanostructures is located at 343 nm, which originates from the recombination of free exciton of electron−hole.[34] However, the peak does not appear in our sample; the observed spectrum shows a strong and dominated green emission at ~524 nm, which is due to the fact that the peaks caused by defects associated with oxygen vacancies or tin interstitials resulting from the size effect of the SnO_2 nanostructures are strong, thereby crippling the band-to-band emission peak.[35] Similar results are also observed by Hu et al. and reported in the literature.[36]

To examine the purity and chemical compositions, we examined the prepared HTNs by FTIR spectroscopy. Figure 2c exhibits the typical FTIR spectrum of the prepared HTNs. Several well-defined absorption peaks are observed in the FTIR spectrum of the HTNs. The presence of a broad absorption peak at ~3421 cm^{-1} is related to the fundamental stretching vibration of hydroxyl groups (free or bonded) which is further confirmed by weak band at about 1627 cm^{-1}. This absorption band is caused by the bending vibration of coordinated H_2O as well as Sn−OH. The strong peak located at around 550−700 cm^{-1} is likely due to the vibration of Sn−O bond in SnO_2 lattice.[37] The peak around at 1110 cm^{-1} is due to the (Sn−OH) vibrations.[38] Thus, the FT-IR spectrum confirmed the presence of Sn−O bonds and OH groups in the HTNs.

To investigate the elemental composition, the prepared HTNs were examined by energy dispersive spectroscopy (EDS) attached with FESEM. Figure 2d exhibits the typical EDS spectrum of the HTNs. The EDS spectrum exhibits the well-defined signals at ~0.25 and 3.45 keV, which can be indexed to L and K lines of the Sn element and O element, respectively. Therefore, the presence of Sn and O in the EDS spectrum confirmed that the prepared the HTNs are SnO_2.

BET nitrogen adsorption−desorption was performed to determine the specific surface area of the as-prepared HTNs. As shown in Figure 2e, a distinct hysteresis loop is observed in the isotherm. Figure 2f exhibits the pore size distributions calculated from the adsorption branch of the nitrogen adsorption−desorption isotherm using the BJH formula. It reveals that the isotherm of the synthesized SnO_2 product is a type IV isotherm with H_3-type hysteresis loops according to IUPAC. The BET surface area of the SnO_2 product is 27.8 $m^2 g^{-1}$, and the larger value may be attributed to the hierarchical morphologies of the prepared material. The narrow size distribution of ~7.8 nm of the prepared HTNs could originate from the gap between the adjacent small nanostructures.

To examine the effect of the experimental parameters on the morphologies and sizes of the as-prepared SnO_2 structures, we performed various experiments. As can be seen from the FESEM images shown in Figure S1a, b in the Supporting Information, small nanosheets are assembled in ball-shaped morphologies when the $SnCl_2{\cdot}2H_2O$ and $C_6H_5Na_3O_7{\cdot}2H_2O$ molar ratio was 0.3. The typical diameter of single ball-shaped morphologies is ~200 nm. When the molar ratio was increased to 0.5, the well-defined hierarchical 3D architectures were obtained (see FigureS1c, d in the Supporting Information). Once the molar ratio was further up to 0.7, over growth in the hierarchical 3D architectures were formed. The typical diameter of the obtained morphologies was ~4 μm (see Figure S1e in the Supporting Information). Interestingly, the secondary growth occurs at the surface of the sheets and many small sheets grew on the surface of the original sheets. These observations suggests that $C_6H_5Na_3O_7{\cdot}2H_2O$ is crucial for the synthesis of the desired hierarchical structures. Although the exact reason how $C_6H_5Na_3O_7{\cdot}2H_2O$ affect the morphology of the prepared materials is not clear yet and hence it is suggested that gradually increasing the amount of $C_6H_5Na_3O_7{\cdot}2H_2O$ could not only facilitate the assembly of pristine materials and lead to the growth of hierarchical structures but also increase the size of the products.

To investigate the detailed formation mechanism of SnO_2 hierarchical structures, time-dependent experiments were also conducted at 180 °C with a fixed precursor concentration ($SnCl_2{\cdot}2H_2O/C_6H_5Na_3O_7{\cdot}2H_2O$ with molar ratio of 0.5). When reaction time was 4 h, the relatively uniform nanosheets were formed (see Figure S2a in the Supporting Information). As the hydrothermal process was prolonged to 8 h, 2D nanosheets further grew (see Figure S2b in the Supporting

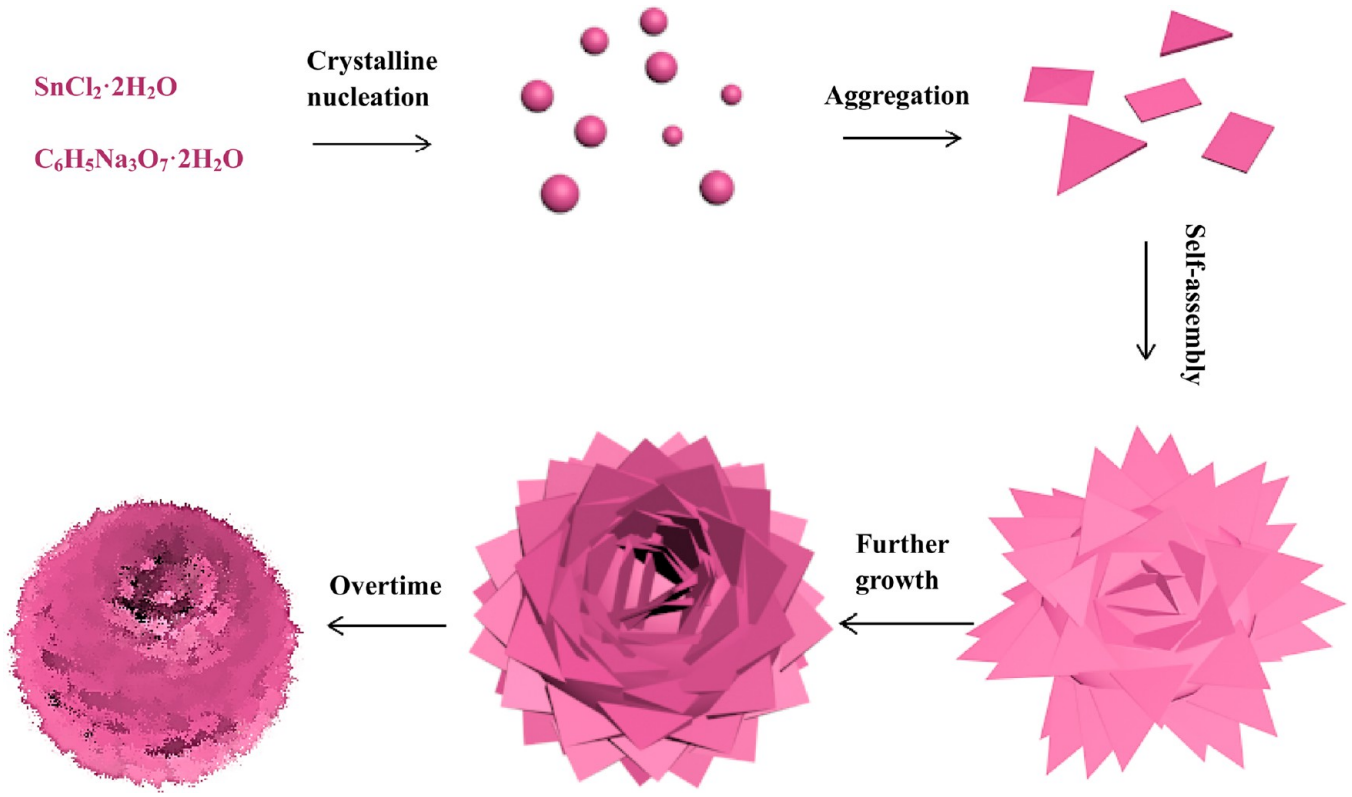

Figure 3. Schematic for the possible growth of the as-synthesized hierarchical SnO_2 nanostructures.

Information). When the reaction time increased to 12 h, high yield and uniform hierarchical SnO_2 nanostructures were produced (see Figure S2c in the Supporting Information). Further, when the reaction time increased up to 16 h, the flowerlike SnO_2 heterostructures are broken (see Figure S2d in the Supporting Information).

On the basis of the above experimental results, a possible growth mechanism for the formation of the HTNs was proposed. Figure 3 shows the schematic for the formation of the HTNs. At first, a large number of tiny primary SnO_2 nanocrystals were formed because of the hydrolysis of $SnCl_2$, whereas in the second step, because of the "oriented attachment" growth process, the grown small SnO_2 nanoparticles are assembled with each other to form nanosheets.[39]Subsequently, the fast oriental attachment of the SnO_2 particles results in the formation of SnO_2 nanosheets. Moreover, because of the surface energy minimization, the new formed particles would spontaneously "land" on the as-formed sheets and further grow to another sheet, thus flowerlike SnO_2 architectures are formed.[40,41]Besides, as a chelating ligand with a strong coordinating ability, sodium citrate can coordinate with tin ions (Sn^{2+}) to form stable hierarchical structures. The formation of the complexes can sharply reduce the availability of free tin ions in aqueous solution, resulting in a slow reaction rate. That is important for the formation of a well-dispersed flowerlike product. However, once the reaction time was further extended, the SnO_2 nanocrystals with larger surface energies have a stronger tendency to dissolve and agglomerate.

3.2. Photocatalytic Degradation of Organic Dyes Using Hierarchical SnO_2 Nanostructures Made of Intermingled Ultrathin Nanosheets. To demonstrate the photocatalytic activities of the synthesized hierarchical SnO_2 nanostructures for the degradation of organic pollutants, we conducted photocatalytic degradation experiments of methylene blue (MB), methyl orange (MO), and rhodamine B (RhB). The initial concentration for all the organic dyes were 40 mg L^{-1}. Figure 4a shows the adsorption spectrum of MB dye over the prepared HTNs measured at each 5 min time interval. As seen from the observed UV−vis, the spectrum that the characteristic absorption peak at ~665 nm decreases gradually with the increasing of the illumination time. Obviously, MB is degraded ~99% when the radiation time reached 20 min. The adsorption spectrum of MO in aqueous solution under the same condition is shown in Figure 4b. It indicates that the concentration of MO is decreased as the irradiation time increasing by measuring the intensity of characteristic absorption peak (465 nm), and MO is degraded 96% after 50 min. Finally, further comparison was made to investigate the photocatalytic activity of SnO_2 products for the degradation of RhB in aqueous solution. The intensity of characteristic adsorption peak (555 nm) of RhB diminished gradually with extension of the exposure time (Figure 4c, decomposing about 97% after 60 min of irradiation. The results suggest that the as-synthesized hierarchical SnO_2 nanostructures exhibited excellent photocatalytic activity toward MB, MO and RhB. Different degradation efficiencies for MB, MO and RhB can be observed directly in Figure 4d. The experimental data show the photocatalytic degradation rate of MB, MO, and RhB is about 99, 64, and 82% after 20 min, respectively.

To compare the photocatalytic efficiency of different morphology and structure, we performed various photocatalytic experiments for the degradation of MB, MO, and RhB in the presence of three different morphologies, i.e., hierarchical SnO_2 nanostructures (sample 1) and microflowers (sample 2[42]). Interestingly, the hierarchical SnO_2 nanostructures exhibited the outstanding photocatalytic performance among all three

dx.doi.org/10.1021/am405301v | ACS Appl. Mater. Interfaces 2014, 6, 2174−2184

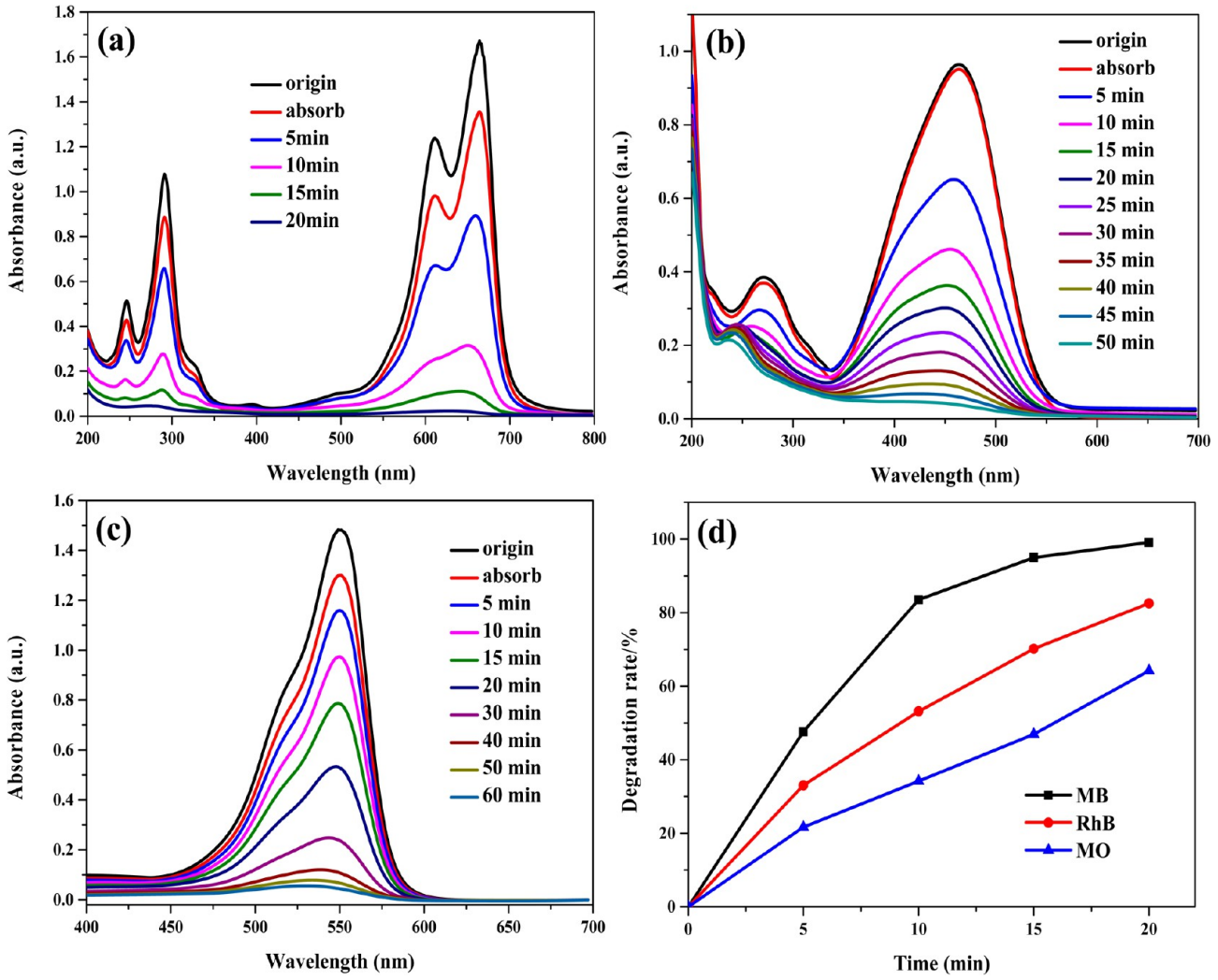

Figure 4. Variations in adsorption spectra of organics dye solution in the presence of the SnO_2 products irradiated by a UV lamp for different time: (a) MB, (b) MO, (c) RhB, and (d) photocatalytic degradation rate of MB, MO, and RhB.

samples, mainly due to the specific morphology, which provide larger specific surface area than the others (table 1).

Table 1. Relevant Parameters of Two Kinds of Photocatalysts with Different Morphologies

		MB		MO		RhB	
	BET surface area (m^2 g^{-1})	time (min)	η (%)	time (min)	η(%)	time (min)	η (%)
sample 1	27.8	20	99	50	96	60	97
sample 2	16.9	60	98	100	97	180	97

In general, during photocatalytic degradation of dye molecules, hydroxyl radicals (·OH) plays a main role.[43] Therefore, increasing the percentage of ·OH in the reaction system can immediately increase the photocatalytic efficiency. On the basis of the photocatalysis mechanism (Figure 5), the ·OH generated from the oxidization of H_2O by photogenerated holes (h^+) and the deoxidization of O_2 by photogenerated electrons (e^-) by UV irradiation.[44] Nevertheless, the photogenerated electrons and holes can recombine easily in the volume or on the surface of the semiconductor.[45] Hence, two ways can be tried to enhance the photocatalytic efficiency of hierarchical SnO_2 nanostructures. First, the decrease in the recombination of the photogenerated electrons and holes allows them to take part in the photocatalytic reaction. Second, optimizing the morphology and structure of the products to get more reactive species, enhances the photocatalytic efficiency.

On the basis of the above analysis, in our experiments, the remarkable photocatalytic activities of SnO_2 microflowers may be attributed to the special hierarchical structure which is consist of nanosheets. This excellent structure can provide more active sites to adsorb more reactive species and O_2 and allow more effective transport for the reactant molecules to get to the active sites. This means that the hierarchical structure can improve the photon application efficiency, thus improving the efficiency of the photocatalysis.

3.3. Gas Sensor Applications of Hierarchical SnO_2 Nanostructures Made of Intermingled Ultrathin Nanosheets. SnO_2 has been proved to be a good sensing material for harmful and toxic gases detection due to its excellent semiconducting and mature fabrication technology.[46] In our study, the gas sensitivity of the obtained hierarchical SnO_2 nanostructures and SnO_2 bulk were fabricated to examine the sensor properties. To study the effect of the operating current, the responses of SnO_2 gas sensors to 50 ppm ethanol as a function of operating current were tested and the results are shown in Figure 6a. It was seen that the sensing response first

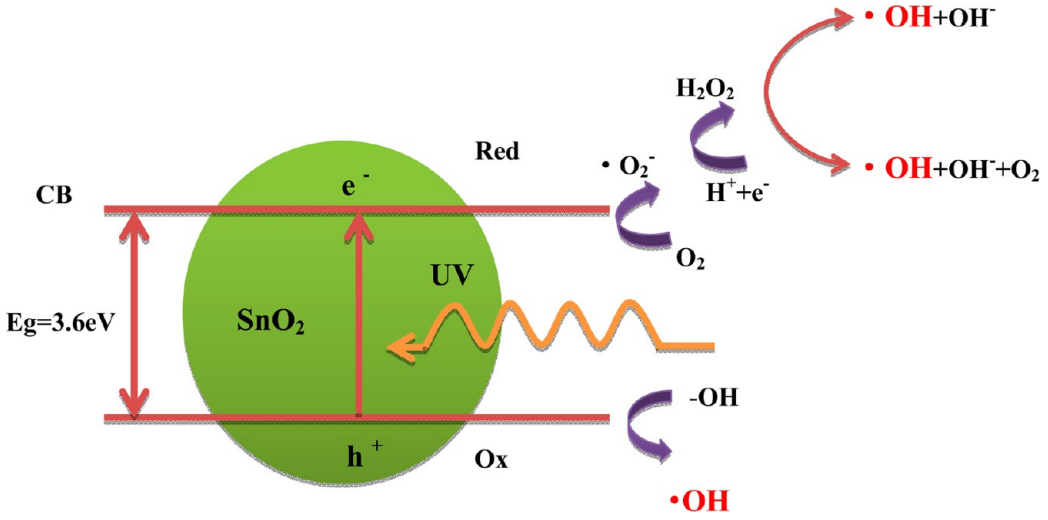

Figure 5. Photocatalytic mechanism of the as-synthesized hierarchical SnO_2 nanostructures.

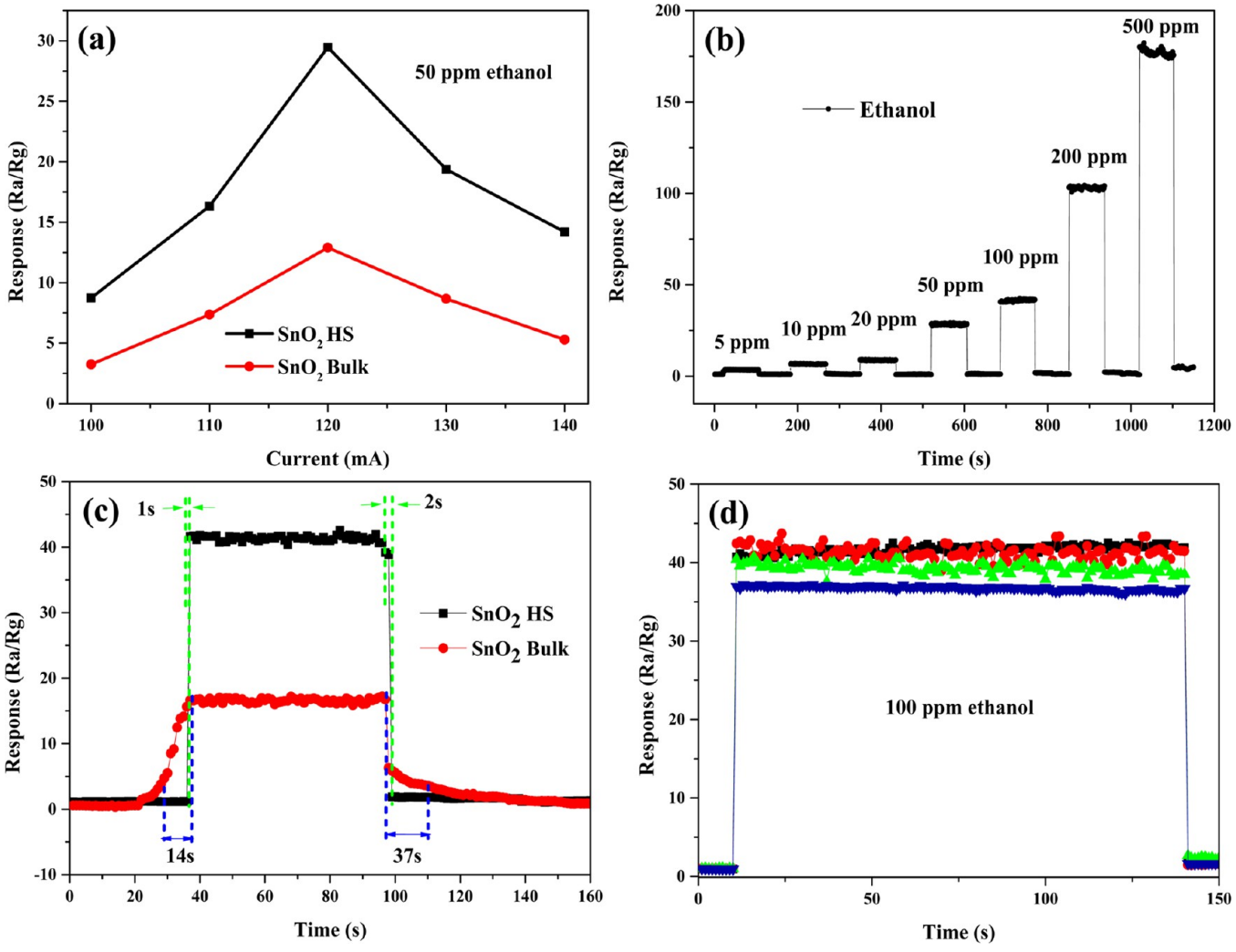

Figure 6. (a) Sensor sensitivity vs operating current of 3D SnO_2 products and SnO_2 bulk exposing 100 ppm ethanol; (b) response of hierarchical SnO_2 nanostructures sensors to ethanol with different concentration; (c) response and recover time of two sensors; (d) repeatability tests of the hierarchical SnO_2 nanostructures sensor at ethanol concentrations of 100 ppm.

increased with current, up to 120 mA, and then decreased. It can be seen that for 100 ppm of ethanol, the maximum response values of two sensors are 29.7 and 13.2 at the optimal current of 120 mA, respectively. Thus the optimized 120 mA was chosen for further gas sensing tests of hierarchical SnO_2 nanostructures. Figure 6b shows the representative dynamic gas

dx.doi.org/10.1021/am405301v | ACS Appl. Mater. Interfaces 2014, 6, 2174−2184

response of SnO_2 gas sensor to ethanol with concentrations ranging from 5 ppm to 500 ppm when the sensor worked at 120 mA. Seven cycles were successively recorded, corresponding to seven different ethanol concentrations of 5, 10, 20, 50, 100, 200, and 500 ppm, respectively. From the curves, it can be seen that the conductance of the sensor undergoes a drastic rise upon the injection of acetone and drops to its initial state after the sensor was exposed to air. The sensitivity of the sensor to 5 ppm ethanol is around 5.13 and that to 500 ppm ethanol is around 183.8. It indicates that the sensing detection limit is rather high for the hierarchical SnO_2 nanostructures. The sensitivity of hierarchical SnO_2 nanostructures to several other compounds (all with the concentrations of 100 ppm) is also studied. The response and recovery time of hierarchical nanostructures to 100 ppm of ethanol at 120 mA are as short as 1 and 2 s, respectively, as shown in Figure 6c, whereas those of bulk structures are 14 and 37 s, respectively. The response and recovery value of the bulk SnO_2 are much longer than that of hierarchical SnO_2 nanostructures. The repeatability has been investigated at ethanol concentrations of 100 ppm and it was found that hierarchical SnO_2 nanostructures exhibited an excellent repeatability as shown in Figure 6d.

Figure 7 exhibits the sensor responses for the hierarchical SnO_2 nanostructures and SnO_2 bulk powder at 120 mA for 100

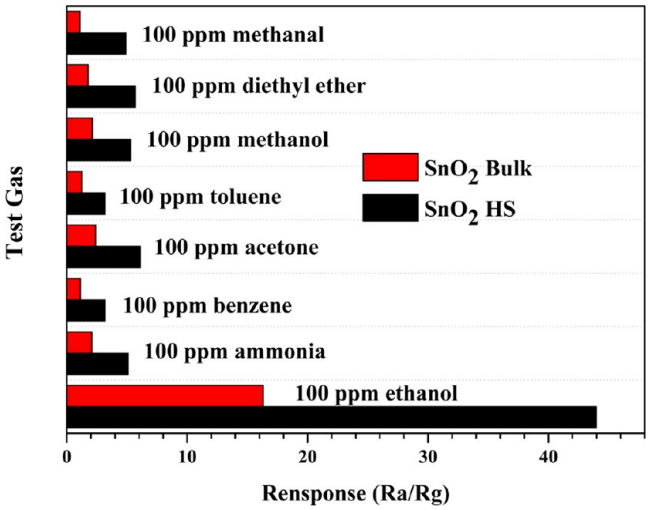

Figure 7. Responses of sensors based on two sensors to various gases.

ppm of various gases, including methanol, Formaldehyde, diethyl ether, methanol, toluene, acetone, benzene, ammonia and ethanol. Clearly, the responses of the hierarchical SnO_2 nanostructures based sensor to eight gases are quick compared with the bulk one, and the largest response is only observed for ethanol with a value of up to 44.7, implying the good selectivity of the sensor for ethanol.

To examine the effect of SnO_2 morphologies toward ethanol gas sensing performances, four different morphologies such as hierarchical SnO_2 nanostructures (sample 1), nanopolyhedrons SnO_2 (sample 2[28]), rattle-type SnO_2 (sample 3[47]), and nanospike SnO_2, (sample 4[48]) were investigated. Table 2 summarizes the comparison of gas-sensing characteristics of gas sensors fabricated by SnO_2 with different morphologies. From the detailed experiments, it is clear that the hierarchical SnO_2 nanostructures exhibited excellent gas sensing properties.

It is well-known that the gas sensing mechanism of metal oxide semiconductor is an adsorption−oxidation−desorption

Table 2. Comparison of Gas-Sensing Characteristics of Gas Sensors Fabricated by SnO_2 with Different Morphologies

	sample 1	sample 2	sample 3	sample 4
response (R_a/R_g)	44	14	17	35

process leading to the change of the conductance of the sensor.[49] When the materials exposed to air, oxygen was adsorbed onto the surface of the SnO_2 nanosheets and ionized to O_2 (ads)$^-$ or O(ads)$^-$ by capturing free electrons from the conduction band of SnO_2, as is shown in eqs 1 and 2

$$O_2(gas) + e^- \rightarrow O_2(ads)^- \quad (1)$$

$$O_2(gas) + e^- \rightarrow 2O(ads)^- \quad (2)$$

The adsorption of $O_2(ads)^-$ and $O(ads)^-$ ions on the surface of SnO_2 nanosheets is vitally important to improve the receptor function of the sensor. When the sensor contact with a reducing gas such as ethanol, these gas molecules could react with adsorbed $O_2(ads)^-$ and $O(ads)^-$ and release the trapped electron to the conduction band, giving rise to the reduction of the resistance.[50]

Besides, the gas sensing properties are also closely related to the structural properties of the materials.[51] The improvement of the sensing performance of the SnO_2 nanostructures may be attributed to the contribution of the contact surface area between the hierarchical structures and the target gases.

3.4. Supercapacitor Applications of Hierarchical SnO_2 Nanostructures Made of Intermingled Ultrathin Nanosheets. The capacitive performance of the as-prepared SnO_2 structures was evaluated by CV and charge−discharge in three-electrode systems. Figure 8a shows the CV curves of SnO_2 nanostructures at various scan rates ranging from 5 to 200 mV s^{-1} in 1 M Na_2SO_4 aqueous electrolyte. The CVs of the SnO_2 electrode are nearly symmetrical even with the scan rate increasing up to 200 mV s^{-1}, indicating the excellent capacitive property and rate capability. A galvanostatic charging/discharging test was also performed with different current densities 1.0, 1.2, 1.5, 2.0, and 5.0 A g^{-1}, as shown in Figure 8b. The linear voltage versus time profiles, the symmetrical charge/discharge characteristics, and a quick I−V response represent good capacitive characteristics for our supercapacitor. The specific capacitances evaluated from the discharge curves were 187.7, 121.6, 115.1, 98.6, and 82.2 F g^{-1} at current densities of 1.0, 1.2, 1.5, 2.0, and 5.0 A g^{-1}, respectively (Figure 8c). Typical Nyquist plots of the electrodes are presented in Figure 8d. From the point intersecting with the real axis in the range of high frequency, the internal resistance of the 3D architectures was evaluated to be approximately 0.32 Ω, manifesting very low internal resistance of the electrode. The results further indicated that the 3D SnO_2 nanostructures are excellent electrode materials for the supercapacitors. Figure 9 demonstrates the cycling performance of the device up to 2000 cycles at the current density of 1.0 A g^{-1}. Almost no obvious specific capacitance loss was observed, indicating its excellent long-term cycling stability. Moreover, the supercapacitor fabricated from the hierarchically SnO_2 structures have shown better properties compared with the same morphology which was reported recently.[52]

The enhanced electrochemical performance could be attributed to the following structural features. First, SnO_2 can absorb electrolyte cations (Na^+) on the electrode surface from electrolyte: $(SnO_2)_{surface} + Na^+ + e^- \leftrightarrow (SnO_2{-}Na^+)_{surface}$,[53]

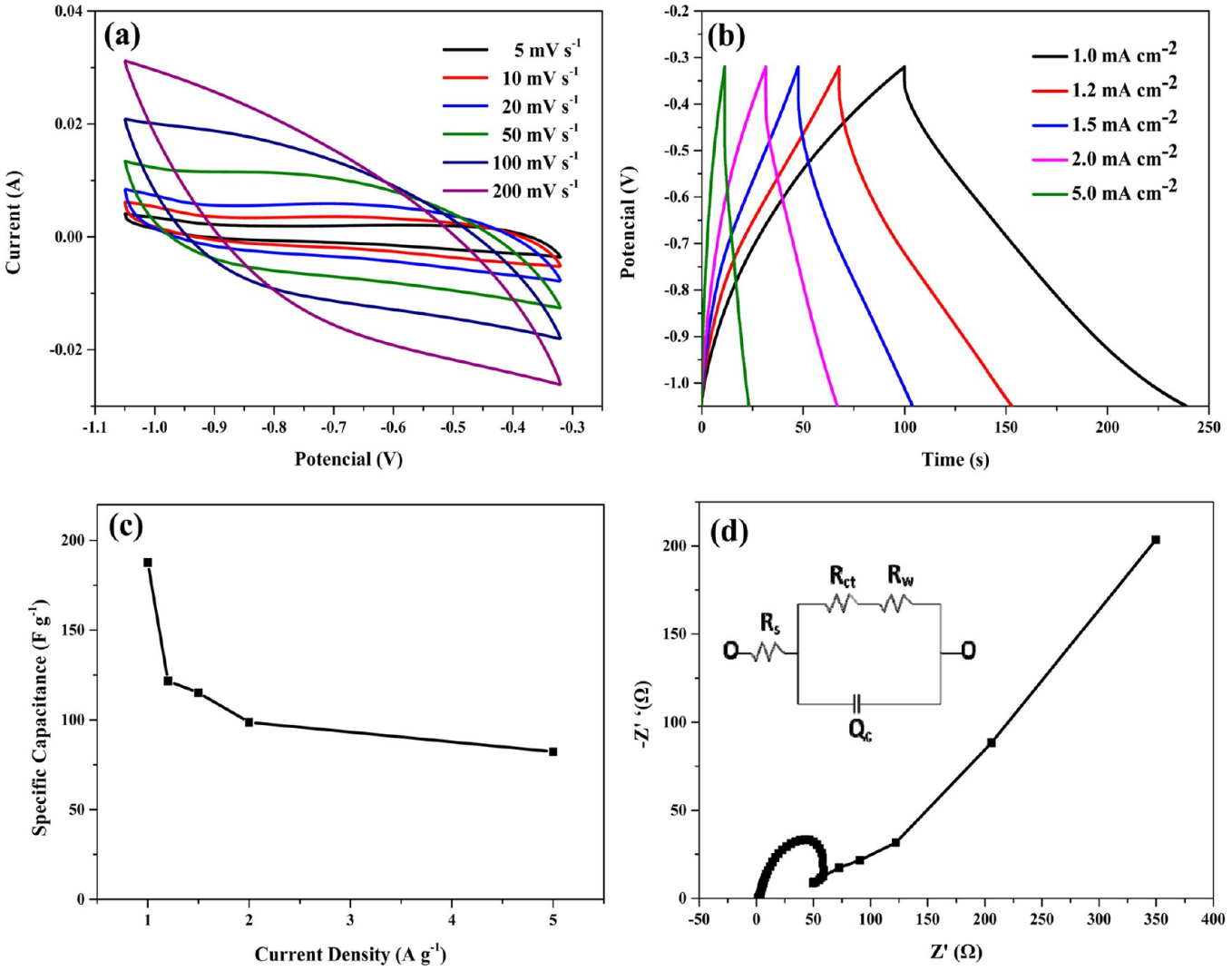

Figure 8. (a) CV curves at scan rates between 5 and 200 mVs^{-1}; (b) charge/discharge curves at current densities ranged from 1.0 to 5.0 Ag^{-1}; (c) current density dependence of the specific capacitance; (d) EIS spectra of the hierarchical SnO_2 nanostructures electrode.

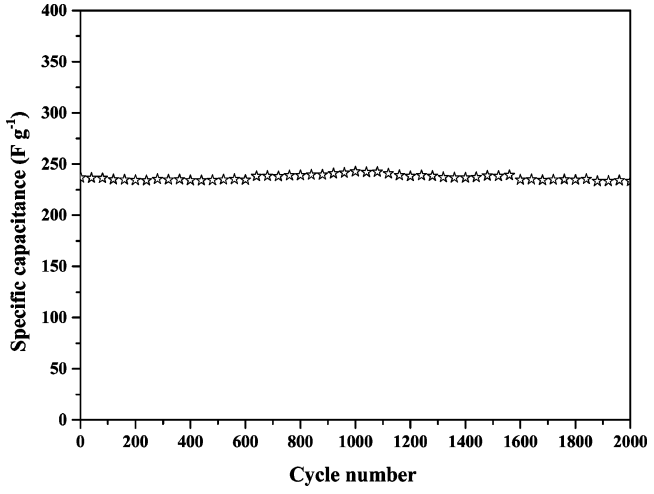

Figure 9. Cycling performance at current density of $1Ag^{-1}$.

providing more charge storage. Second, the easy access of SO_3^{2-} by the SnO_2 microspheres can be guaranteed by the hierarchical nature and thin thickness of the nanosheets. Therefore, both Na^+ and SO_3^{2-} from the electrolyte are fully utilized in SnO_2 electrode.

CONCLUSIONS

In summary, a facile and simple method has been developed for preparing 3D hierarchical SnO_2 nanostructures. The prepared 3D hierarchical architectures were made of intermingled ultrathin nanosheets. It was found that the concentrations of the precursor and reaction time play important role to control the morphologies and sizes of the prepared product. The prepared hierarchical SnO_2 nanostructures were used as efficient photocatalyst and exhibit substantial degradation for three different organic dyes, i.e., MB, MO ,and RhB. The substantial degradation of the dyes was mainly due to specific morphologies of the prepared material. The prepared hierarchical nanomaterials were efficiently be used for the fabrication of high-sensitive and selective ethanol gas sensors. Finally, the prepared hierarchical SnO_2 nanostructures provide fast ion and electron transfer, which lead to a prominent supercapacitor performance. This work demonstrates that the simply prepared SnO_2 nanomaterials can efficiently be used as a photocatalyst, gas sensing material, and supercapacitor applications.

dx.doi.org/10.1021/am405301v | ACS Appl. Mater. Interfaces 2014, 6, 2174−2184

■ ASSOCIATED CONTENT

Supporting Information

The precursor concentration and time-dependent SEM images of SnO_2 nanostructures. This material is available free of charge via the Internet at http://pubs.acs.org

■ AUTHOR INFORMATION

Corresponding Authors

*E-mail: wuxiang05@gmail.com.
*E-mail: ahmadumar786@gmail.com.

Notes

The authors declare no competing financial interest.

■ ACKNOWLEDGMENTS

This work was supported by the Foundation for Key Project of Ministry of Education, China (211046), Open Fund of State Key Laboratory for Modification of Chemical Fibers and Polymer Materials, Dong Hua University (K1012), Program for New Century Excellent Talents in Heilongjiang Provincial University (1252-NCET-018), the Scientific Research Fund of Heilongjiang Provincial Education Department (12531179) and Program for Scientific and Technological Innovation Team Construction in Universities of Heilongjiang (2011TD010). Ahmad Umar would like to acknowledge the support of the Ministry of Higher Education, Kingdom of Saudi Arabia under the Promising Centre for Sensors and Electronic Devices (PCSED) project (PCSED-002-11) at Najran University, Kingdom of Saudi Arabia.

■ REFERENCES

(1) Ahmad, Umar, Ed.; Hahn, Y. B. *Metal Oxide Nanostructures and Their Applications*; American Scientific: Los Angeles, CA, 2010.
(2) Fang, X. S.; Zhai, T. Y.; Gautam, U. K.; Li, L.; Wu, L. M.; Bando, Y.; Golberg, D. *Prog. Mater. Sci.* **2011**, *56*, 175−287.
(3) Xi, G. C.; Ye, J. H. *Inorg. Chem.* **2010**, *49*, 2302−2309.
(4) Han, Y. T.; Wu, X.; Ma, Y. L.; Gong, L. H.; Qu, F. Y.; Fan, H. J. *CrystEngComm.* **2011**, *13*, 3506−3510.
(5) Zhang, Z. L.; Song, H. Y.; Zhang, S. S.; Zhang, J. Y.; Bao, W. Y.; Zhao, Q. Q; Wu, X. *CrystEngComm.* **2014**, *16*, 110−115.
(6) Jia, B. X.; Jia, W. N.; Ma, Y. L.; Wu, X.; Qu, F. Y. *Sci. Adv. Mater.* **2012**, *4*, 702−707.
(7) Jia, B. X.; Jia, W. N.; Wu, X.; Qu, F. Y. *RSC Adv.* **2013**, *3*, 12140−12148.
(8) Lee, S. C.; Kim, S. Y.; Lee, W. S.; Jung, S. Y.; Hwang, B. W.; Ragupathy, D.; Lee, D. D.; Lee, S. Y.; Kim, J. C. *Sensors* **2011**, *11*, 6893−6904.
(9) Lu, T.; Zhang, Y. P.; Li, H. B.; Pan, L. K.; Li, Y. L.; Sun, Z. *Electrochim. Acta* **2010**, *55*, 4170−4173.
(10) Yan, J.; Khoo, E.; Sumboja, A.; Lee, P. S. *ACS Nano* **2010**, *4*, 4247−4255.
(11) Chen, J. S.; Archer, L. A.; Lou, X. W. *J. Mater. Chem.* **2011**, *21*, 9912−9924.
(12) Hou, X. J.; Liu, B.; Wang, X. F.; Wang, Z. R.; Wang, Q. F.; Chen, D.; Shen, G. Z. *Nanoscale* **2013**, *5*, 7831−7837.
(13) Liu, Y.; Jiao, Y.; Yin, B. S.; Zhang, S. W.; Qu, F. Y.; Wu, X. *Nano-Micro Lett.* **2013**, *5*, 234−241.
(14) Zhang, Z. Y.; Zou, R. J.; Song, G. S.; Yu, L.; Chen, Z. G.; Hu, J. Q. *J. Mater. Chem.* **2011**, *21*, 17360−17365.
(15) Zou, R. J.; Zhang, Z. Y.; Jiang, L.; Xu, K. B.; Tian, Q. W.; Xue, S. L.; Hu, J. Q.; Bando, Y.; Golberg, D. *J. Mater. Chem.* **2012**, *22*, 19196−19201.
(16) Shan, H.; Liu, C. B.; Liu, L.; Zhang, J. B.; Li, H. Y.; Liu, Z.; Zhang, X. B. *ACS Appl. Mater. Interfaces* **2013**, *5*, 6376−6380.
(17) Hu, J. Q.; Chen, Z. G.; Zou, R. J.; Sun, Y. G. *CrystEngComm* **2010**, *12*, 89−93.
(18) Han, Y. T.; Wu, X.; Shen, G. Z.; Dierre, B.; Gong, L. H.; Qu, F. Y.; Bando, Y.; Sekiguchi, T.; Fabbri, F.; Golberg, D. *J. Phys. Chem. C* **2010**, *114*, 8235−8240.
(19) Guo, J.; Zhang, J.; Ju, D. X.; Xu, H. Y.; Cao, B. Q. *Powder Technol.* **2013**, *250*, 40−45.
(20) Wang, M.; Gao, Y.; Dai, L.; Cao, C.; Chen, Z.; Guo, X. *Sci. Adv. Mater.* **2013**, *5*, 1867−1876.
(21) Meng, X. Q.; Zhou, M.; Li, X. L.; Yao, J. Y.; Liu, F. L.; He, H. C.; Xiao, P.; Zhang, Y. H. *Electrochim. Acta* **2013**, *109*, 20−26.
(22) Chen, A.; Peng, X.; Koczkur, K.; Miller, B. *Chem. Commun.* **2004**, *17*, 1964−1965.
(23) Zhang, Y.; Yu, K.; Li, G.; Peng, D.; Zhang, Q.; Xu, F.; Bai, W.; Ouyang, S.; Zhu, Z. *Mater. Lett.* **2006**, *60*, 3109−3112.
(24) Ghosh, S.; Das, K.; Chakrabarti, K.; De, S. K. *CrystEngComm* **2012**, *14*, 927−932.
(25) Wang, J.; Qu, F. Y.; Wu, X. *Sci. Adv. Mater.* **2013**, *5*, 1052−1059.
(26) Liu, J. P.; Cheng, C. W.; Zhou, W. W.; Li, H. X.; Fan, H. J. *Chem. Commun.* **2011**, *47*, 3436−3438.
(27) Li, Z. P.; Zhao, Q. Q.; Fan, W. L.; Zhan, J. H. *Nanoscale* **2011**, *3*, 1646−1652.
(28) Chen, D.; Xu, J.; Xie, Z.; Shen, G. Z. *Appl. Mater. Interfaces* **2011**, *3*, 2112−2117.
(29) Pusawale, S. N.; Deshmukh, P. R.; Lokhande, C. D. *Appl. Surf. Sci.* **2011**, *257*, 9498−9452.
(30) Wei, R. H.; Du, K.; Gong, X. Y.; Chen, Q. D.; Tang, Z. X.; You, J. H.; Li, L. B.; Yang, H. B. *Appl. Surf. Sci.* **2009**, *255*, 6464−6468.
(31) Cheng, G.; Wang, J. M.; Liu, X. W.; Huang, K. X. *J. Phys. Chem. B* **2006**, *110*, 16208−16211.
(32) Cheng, B.; Russell, J. M.; Shi, W. S.; Zhang, L.; Samulski, E. T. *J. Am. Chem. Soc.* **2004**, *126*, 5972−5973.
(33) Chen, H. T.; Wu, X. L.; Zhang, Y. Y.; Zhu, J.; Cheng, Y. C.; Chu, P. K. *Appl. Phys. A: Mater. Sci. Process* **2009**, *97*, 581−584.
(34) Lee, E. J. H.; Ribeiro, C.; Giraldi, T. R.; Longo, E.; Leite, E. R. *Appl. Phys. Lett.* **2004**, *84*, 1745−1747.
(35) Kimand, T. W.; Lee, D. U. *J. Appl. Phys.* **2000**, *88*, 3759−3761.
(36) Hu, J. Q.; Bando, Y.; Golberg, D. *Chem. Phys. Lett.* **2003**, *372*, 758−762.
(37) Karuppuchamy, S.; Jeong, J. M. *J. Oleo Sci.* **2006**, *55*, 263−266.
(38) Abello, L.; Bochu, B.; Gaskov, A.; Koudryavtseva, S.; Lucazeau, G.; Roumyantseva, M. *J. Solid State Chem.* **1998**, *135*, 78−83.
(39) Li, D. S.; Nielsen, M. H.; Lee, J. R. I.; Frandsen, C.; Banfield, J. F.; De Yoreo, J. J. *Science* **2012**, *336*, 1014−1018.
(40) Penn, R. L.; Banfield, J. F. *Science* **1998**, *281*, 969−971.
(41) Banfield, J. F.; Welch, S. A.; Zhang, H. Z.; Ebert, T. T.; Penn, R. L *Science* **2000**, *289*, 751−754.
(42) Jia, B. X.; Jia, W. N.; Ma, Y. L.; Wu, X.; Qu, F. Y. *Sci. Adv. Mater.* **2012**, *4*, 1127−1132.
(43) Wang, J.; Fan, X. M.; Tian, K.; Zhou, Z. W.; Wang, Y. *Appl. Surf. Sci.* **2011**, *257*, 7763−7770.
(44) Kong, M.; Li, Y. Z.; Chen, X.; Tian, T. T.; Fang, P. F.; Zheng, F.; Zhao, X. J. *J. Am. Chem. Soc.* **2011**, *133*, 16414−16417.
(45) Cheng, H. F.; Huang, B. B.; Dai, Y.; Qin, X. Y.; Zhang, X. Y. *Langmuir* **2010**, *26*, 6618−6624.
(46) Lee, J. H. *Sens. Actuators, B* **2009**, *140*, 319−336.
(47) Wang, L. L.; Fei, T.; Deng, J. N.; Lou, Z.; Wang, R.; Zhang, T. *J. Mater. Chem.* **2012**, *22*, 18111−18114.
(48) Xu, J.; Li, Y. S.; Huang, H. T.; Zhu, Y. G.; Wang, Z. R.; Xie, Z.; Wang, X. F.; Chen, D.; Shen, G. Z. *J. Mater. Chem.* **2011**, *21*, 19086−19092.
(49) Wang, D.; Hu, P.; Xu, J. Q.; Dong, X. W.; Pan, Q. Y. *Sens. Actuators, B* **2009**, *140*, 383−189.
(50) Xiao, L. S.; Shen, H.; Hagen, R.; Pan, J.; Belkoura, L.; Mathur, S. *Chem.Commun.* **2010**, *46*, 6509−6511.
(51) Li, C. C.; Yin, X. M.; Li, Q. H.; Wang, T. H. *CrystEngComm.* **2011**, *13*, 1557−1563.
(52) Jiang, H.; Li, C. Z.; Sun, T.; Ma, Jan. *Nanoscale* **2012**, *4*, 807−812.
(53) Mane, R. S.; Chang, J.; Ham, D.; Pawar, B. N.; Ganesh, T.; Cho, B. W.; Lee, J. K.; Han, S. H. *Curr. Appl. Phys.* **2009**, *9*, 87−91.